

# C-DiffSET: Leveraging Latent Diffusion for SAR-to-EO Image Translation with Confidence-Guided Reliable Object Generation

Jeonghyeok Do

KAIST

ehwjdgur0913@kaist.ac.kr

Jaehyup Lee<sup>†</sup>

KNU

jaehyuplee@knu.ac.kr

Munchurl Kim<sup>†</sup>

KAIST

mkimee@kaist.ac.kr

[https://kaist-viclab.github.io/C-DiffSET\\_site](https://kaist-viclab.github.io/C-DiffSET_site)



Figure 1. Qualitative comparison of SAR-to-EO image translation (SET) results for very recent methods and our proposed C-DiffSET. The first row shows the SET results for full-polarization (HH, HV, VH, and VV) SAR input (ground sample distance (GSD) = 0.5m) of SpaceNet6 dataset, while the second and third rows exhibit the SET results for single-polarization (HH or VV) SAR input (GSD = 1m) of SAR2Opt and QXS-SAROPT datasets, respectively. As shown, our proposed C-DiffSET achieves superior structural accuracy and visual fidelity compared to very recent methods. Note that (i) the SET results for SpaceNet6 show better visual qualities than those of SAR2Opt and QXS-SAROPT because of using the full-polarization SAR input of SpaceNet6, and (ii) the SET results for SAR2Opt are of relatively higher visual qualities than those for QXS-SAROPT due to their less noisy SAR samples of SAR2Opt.

## Abstract

Synthetic Aperture Radar (SAR) imagery provides robust environmental and temporal coverage (e.g., during clouds, seasons, day-night cycles), yet its noise and unique structural patterns pose interpretation challenges, especially for non-experts. SAR-to-EO (Electro-Optical) image translation (SET) has emerged to make SAR images more perceptually interpretable. However, traditional approaches

trained from scratch on limited SAR-EO datasets are prone to overfitting. To address these challenges, we introduce Confidence Diffusion for SAR-to-EO Translation, called C-DiffSET, a framework leveraging pretrained Latent Diffusion Model (LDM) extensively trained on natural images, thus enabling effective adaptation to the EO domain. Remarkably, we find that the pretrained VAE encoder aligns SAR and EO images in the same latent space, even with varying noise levels in SAR inputs. To further improve pixel-wise fidelity for SET, we propose a confidence-guided diffusion (C-Diff) loss that mitigates artifacts from temporal

<sup>†</sup>Co-corresponding authors (equal advising).

discrepancies, such as appearing or disappearing objects, thereby enhancing structural accuracy. C-DiffSET achieves state-of-the-art (SOTA) results on multiple datasets, significantly outperforming the very recent image-to-image translation methods and SET methods with large margins.

## 1. Introduction

Satellite imagery plays a critical role in various applications, including surveillance, transportation, agriculture, disaster assessment, and environmental monitoring [4, 12, 42, 52, 60, 68, 71, 84]. A significant portion of these applications relies on Electro-Optical (EO) imagery, which provides multi-spectral data captured by EO sensors. However, a fundamental limitation of EO imagery is its susceptibility to weather and lighting conditions, reducing its usability in scenarios such as cloudy weather or nighttime. In contrast, Synthetic Aperture Radar (SAR) offers robust sensing capabilities under all weather conditions without the need for light, making it ideal for nighttime operations. Despite these advantages, SAR imagery is generally very difficult to directly interpret the structural and contextual information due to the very different nature of its image structures with high speckle noises [8, 13, 57, 81], unlike the natural color images. Therefore, for easy interpretation and downstream tasks such as target detection and recognition [14, 39–41, 62] developed for natural color images or satellite EO-RGB images, the SAR-to-EO image translation (SET) [15, 25, 28, 31, 32, 50, 54, 76] has been demanded for the usability expansion for SAR image applications. In SET, most existing approaches, including ours, focus on generating RGB bands of EO images [15, 25, 28, 50, 54, 76], as RGB representations are widely used for both human perception and vision-based deep learning models. Therefore, the SET problem in this paper is focused on generating the RGB bands of EO images for SAR input images.

Recent advancements [15, 25, 28, 31, 32, 50, 54, 76] have demonstrated the potential of generating EO-like outputs from SAR images, offering improved textures and enhanced color information. However, several challenges persist: (i) The domain gap between SAR and EO images makes SET an ill-posed problem; (ii) The misalignment between SAR and EO datasets is prone to occur due to their different sensor platforms, satellite positioning shifts, or acquisition conditions, as shown in Fig. 2; (iii) Temporal discrepancies occur due to different acquisition times, also resulting in the spatial misalignment with differences in object appearance and seasons. This makes it very complicated the SET problem (Fig. 2); (iv) Finally, the scarcity of paired SAR-EO datasets makes it challenging for existing methods to learn the SET effectively, often leading to overfitting or unstable results.

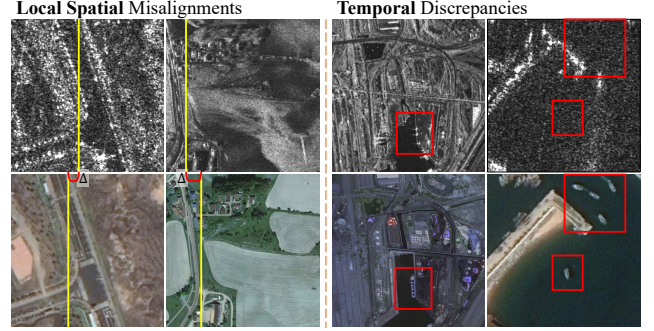


Figure 2. Examples of misalignments and discrepancies in paired SAR-EO datasets. *Left*: Local spatial misalignments caused by sensor differences or acquisition conditions. *Right*: Temporal discrepancies where objects (e.g., ships) appear or disappear between SAR and EO images due to their different acquisition times.

To address these limitations, we *firstly* propose a novel framework that leverages a *pretrained* Latent Diffusion Model (LDM) [11, 47] to improve SAR-to-EO image translation, which is denoted as Confidence Diffusion for SAR-to-EO Translation (C-DiffSET). The advantages of utilizing the pretrained LDM for SET tasks are as follows: (i) Since RGB bands of EO images share visual characteristics with natural images, we fine-tune the pretrained LDM—trained on large-scale natural image datasets—to transfer its representation power to the SET task. This addresses the issue of limited SAR-EO paired data, as our framework can leverage the pretrained knowledge from natural image distributions; (ii) The pretrained LDM operates in a 1/8-downsampled latent space, inherently alleviating spatially local misalignments caused by imperfect alignment processes; (iii) The variational auto-encoder (VAE) [29] from LDM can also be applicable for SAR images. As shown in Fig. 4, despite the presence of significant speckle noise in SAR data, the VAE encoder effectively embeds SAR images into the same latent space as EO images, leveraging its denoising capability. This enables the smooth transfer of SAR latents as conditioning information in the reverse diffusion process, ensuring the generation of EO outputs with accurate pixel-wise correspondence to the SAR inputs.

In addition to utilizing the pretrained LDM as a foundation model for our SET task, we introduce a confidence-guided diffusion (C-Diff) loss to handle temporal discrepancies. The temporal discrepancies, such as objects appearing in only one modality, can introduce artifacts and hallucinated content in the generated EO images. Since these discrepancies originate from real-world acquisition conditions that SAR and EO images are often obtained for same regions at different time instances, they cannot be explicitly corrected in the dataset itself during the training process. To mitigate this, the U-Net [48] in our framework predicts both each predicted noise and its corresponding confidence map, which quantifies the pixel-wise uncertainty in the pre-



dicted noise. The U-Net receives a channel-wise concatenated SAR and noisy EO features as input, allowing it to jointly model both contexts. This setup enables the confidence map to reflect the inherent uncertainty caused by temporal discrepancies, guiding the C-Diff loss to adaptively reduce penalties in regions where SAR-EO discrepancies likely occur. As a result, the generated EO images achieve high pixel-wise fidelity while minimizing artifacts and hallucinations. Our key contributions are summarized as:

- We propose C-DiffSET, the *first* framework to fine-tune a *pretrained* LDM for SET tasks, effectively leveraging their learned representations to overcome the scarcity of SAR-EO image pairs. In the C-DiffSET, SAR and EO images are embedded into the same latent space to ensure pixel-wise correspondence between SAR and EO latent throughout the framework;
- We introduce a novel C-Diff loss that can guide our C-DiffSET to reliably predict both EO outputs and confidence maps for accurate SET to mitigate locally mismatching challenges from temporal discrepancy due to their different acquisition times;
- We validate our C-DiffSET through extensive experiments on datasets with varying resolutions and ground sample distances (GSD) [61], including QXS-SAROPT [19], SAR2Opt [83], and SpaceNet6 [56] datasets, demonstrating the superiority of our C-DiffSET that *significantly* outperforms the very recent image-to-image translation methods and SET methods with *large* margins.

## 2. Related Work

### 2.1. Image-to-Image Translation

Image-to-image translation has been widely studied in various fields, such as image colorization [78, 79], style transfer [24, 55, 87], and image inpainting [22, 44]. These models typically rely on carefully constructed paired datasets across domains for effective training. For instance, Pix2Pix [24] introduced conditional GANs with an  $l_1$  loss for domain-specific translations. However, acquiring paired datasets remains challenging, and various methods have been proposed to work around unpaired data constraints [1, 6, 7, 20, 27, 35]. CycleGAN [87] addressed this limitation using a cycle-consistency loss to facilitate training without paired data. Further addressing non-bijective translation, StegoGAN [70] introduced steganography into GAN-based models, enhancing semantic consistency in cases of domain mismatch by reducing spurious features in generated images without additional supervision.

**Diffusion-based approaches.** Diffusion models [18, 47] have gained significant traction in image-to-image translation due to their ability to model complex data distributions through iterative denoising. Traditional Denoising Diffusion Probabilistic Models (DDPMs) [18] perform diffusion

directly in the pixel space, but their high computational cost limits scalability in high-resolution tasks. To address this, Latent Diffusion Models (LDMs) [47] move the diffusion process to a learned latent space, significantly reducing memory and computational overhead while preserving high-resolution details. Palette [49] employs conditional DDPMs in the pixel domain for high-quality translations, whereas BBDM [33] performs diffusion directly in the latent space, eliminating the need for separate noise conditioning but imposing strict pixel-wise alignment requirements. DGDM [72] extends BBDM with a deterministic translator network to generate target features before diffusion, adding computational overhead and dependency on the translator’s performance. ControlNet [77] and its variants, Uni-ControlNet [82], extend pretrained diffusion models by injecting control signals through additional conditioning networks. These methods excel at preserving structural guidance for simple condition images, such as edge maps or skeleton poses. However, they are less suitable for the SET task, where the relationship between SAR and EO images is highly complex and requires learning intricate domain mappings rather than simple structural constraints.

### 2.2. SAR-to-EO Image Translation (SET)

Deep learning-based image-to-image translation methods [1, 20, 22, 24, 33, 35, 55, 85] have been widely adopted to remote sensing applications, including SAR-to-EO image translation (SET). However, SAR imagery poses unique challenges due to inherent characteristics like speckle noise from backscattering effects [8, 13, 21, 57, 59, 75, 81], complicating the translation process. To address these challenges, most SET studies employ GAN-based approaches [5, 9, 25, 30, 32, 34, 52, 64, 67, 73, 76]. Conditional GAN-based models are commonly used to leverage noisy SAR information as a conditioning input, while CycleGAN-based models align the SAR and EO domains by enforcing cycle-consistency constraints. SAR-SMTNet [73] introduced a Swin-Transformer-based [36] generator to improve structural consistency in SAR-to-EO translation. Additionally, CFCA-SET [31] proposed a coarse-to-fine SAR-to-EO model that incorporates near-infrared (NIR) images during training to refine EO generation.

**Diffusion-based approaches.** Recently, a limited number of diffusion-based studies have been explored for SET, primarily divided into DDPM-based [2, 3] and LDM-based [15, 28, 54] methods. DSE [54] utilize the BBDM [33] to generate EO predictions for downstream tasks like flood segmentation. Expanding on this, cBBDM [28] integrates SAR inputs as conditional information in BBDM to improve translation quality, while CM-Diffusion [15] further enhances BBDM by conditioning on color features, helping to preserve spectral consistency in EO generation.

Despite these advancements, both GAN-based and

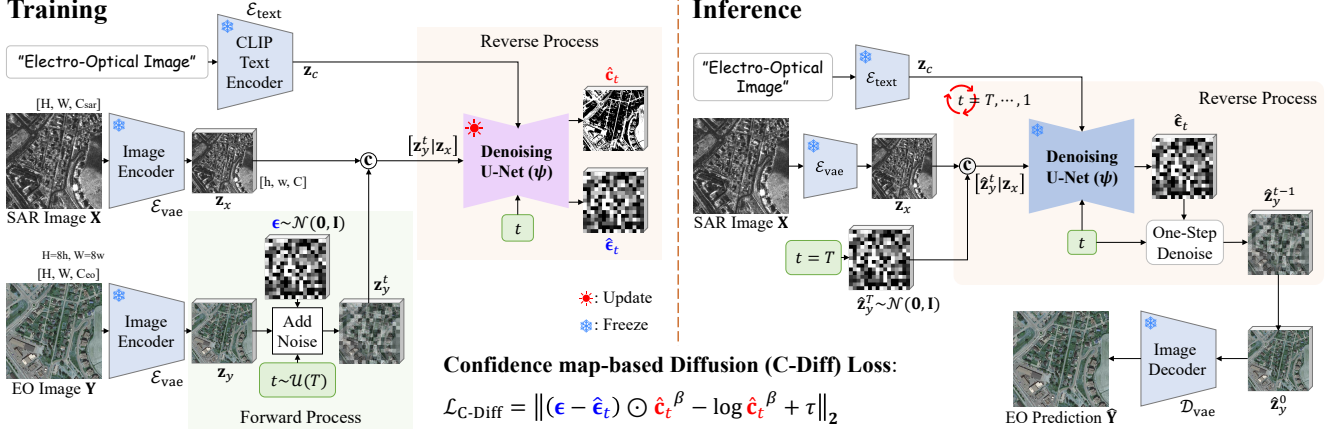


Figure 3. Overall framework of our Confidence Diffusion for SAR-to-EO Translation (C-DiffSET).

diffusion-based methods encounter limitations stemming from the scarcity of paired SAR-EO datasets. The GAN-based models frequently face with convergence challenges and mode collapse under limited data, while diffusion-based approaches struggle with overfitting and slow convergence due to extensive training from scratch. Recent open-source [63] releases of foundation LDMs, such as Stable Diffusion [11, 47] and SDXL [45], pretrained on large-scale text-to-image datasets (e.g., LAION-5B [51]), have demonstrated strong generative priors for image synthesis. These models have been widely adapted for natural image applications [16, 26, 69, 74], showcasing their flexibility in domain adaptation. Building on this foundation, we fine-tune a pre-trained LDM for the SET task. By using the extensive visual representations learned from large-scale generative models, C-DiffSET effectively adapts to SAR-EO data, achieving robust translation while mitigating the risk of overfitting.

### 3. Methods

#### 3.1. Overview of Proposed C-DiffSET

We utilize a paired SAR-EO dataset  $\mathcal{I} = \{(\mathbf{X}, \mathbf{Y})\}$ , where  $\mathbf{X} \in \mathbb{R}^{H \times W \times C_{\text{sar}}}$  represents SAR images of  $H \times W$  sizes and  $C_{\text{sar}}$  channels and  $\mathbf{Y} \in \mathbb{R}^{H \times W \times C_{\text{eo}}}$  denotes EO images of  $H \times W$  sizes and  $C_{\text{eo}}$  channels. Our goal is to generate a predicted EO image  $\hat{\mathbf{Y}}$  corresponding to the given SAR input  $\mathbf{X}$ . Fig. 3 illustrates the proposed Confidence Diffusion for SAR-to-EO Translation (C-DiffSET) framework, which comprises three key components: (i) the embedding of SAR and EO images into the latent space, (ii) the forward diffusion process, and (iii) the reverse diffusion process with the confidence-guided diffusion (C-Diff) loss. As described in Sec. 3.2, SAR image  $\mathbf{X}$  and EO image  $\mathbf{Y}$  are passed through the VAE encoder  $\mathcal{E}_{\text{vae}}$ , generating the latent features  $\mathbf{z}_x \in \mathbb{R}^{h \times w \times C}$  (SAR feature) and  $\mathbf{z}_y \in \mathbb{R}^{h \times w \times C}$  (EO feature). In the forward diffusion process (Sec. 3.3), noise  $\epsilon$  is added to the EO feature  $\mathbf{z}_y$  over timesteps  $t$ .

During the reverse diffusion process, the U-Net  $\psi$  takes the noisy EO feature  $\mathbf{z}_y^t$ , the timestep  $t$ , and the SAR feature  $\mathbf{z}_x$  as conditional inputs. The Denoising U-Net  $\psi$  predicts both the noise  $\hat{\epsilon}_t$  and a confidence map  $\hat{c}_t$  that quantifies pixel-wise uncertainty of the prediction. Finally, in Sec. 3.4, we describe the inference stage, where the predicted EO image  $\hat{\mathbf{Y}}$  is generated by reversing the noise-added process.

#### 3.2. SAR and EO Latent Space Generation

We utilize the pretrained VAE from LDM for mapping input images from the pixel space to the latent space. The VAE is frozen during our experiments and serves as both an encoder  $\mathcal{E}_{\text{vae}}$  and a decoder  $\mathcal{D}_{\text{vae}}$  for input images. Since the LDM has been pretrained on large-scale natural image datasets, the VAE is designed to accept 3-channel RGB images as input. Fig. 4 shows the results of applying the VAE encoder  $\mathcal{E}_{\text{vae}}$  and decoder  $\mathcal{D}_{\text{vae}}$  to SAR and EO images, validating its applicability for both modalities.

**EO latent space.** Since the RGB bands of EO images  $\mathbf{Y}$  are naturally represented as 3-channel inputs, they are directly passed through the VAE without modification. In our experiments, we confirmed that the reconstruction error  $\|\mathbf{Y} - \mathcal{D}_{\text{vae}}(\mathcal{E}_{\text{vae}}(\mathbf{Y}))\|_2$  is minimal, ensuring that the VAE accurately preserves the content and structure of EO images. Furthermore, this low reconstruction error indicates that the RGB bands of EO images exhibit minimal domain gap compared to natural RGB images, making them well-suited for adaptation using pretrained LDMs. This indicates that the VAE’s output provides an upper bound on the achievable performance of our framework, serving as a stable baseline for EO image generation.

**SAR latent space.** SAR data  $\mathbf{X}$ , depending on the satellite sensors, is available as single-polarization SAR images of 1-channel (HH or VV component) or full-polarization ones of 4-channel (HH, HV, VH, and VV components). For 1-channel SAR images, we repeat the channel three times to match the VAE’s input requirements. For 4-channel SAR



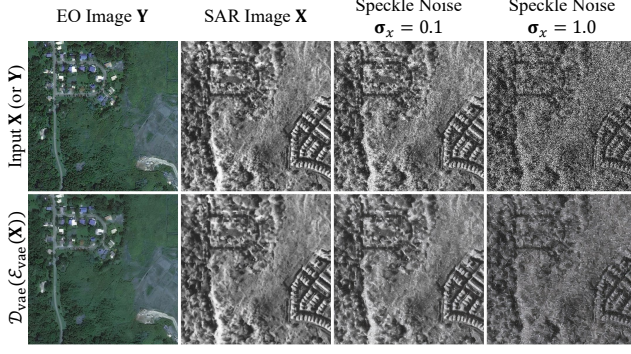


Figure 4. Results of applying the VAE encoder and decoder from LDM to EO and SAR images. The first row shows input images, including EO and SAR images with different levels of speckle noise. The second row presents the corresponding VAE reconstructions, illustrating that both EO and SAR images are accurately reconstructed despite noise variations.

data, we construct a 3-channel input by using HH, the average of HV and VH, and VV components. After passing these inputs through the VAE, we observed that the reconstruction error  $\|\mathbf{X} - \mathcal{D}_{\text{vae}}(\mathcal{E}_{\text{vae}}(\mathbf{X}))\|_2$  remained low, and the outputs appeared visually pleasing, as shown in Fig. 4. Additionally, we examined the VAE’s behavior under varying levels of speckle noise added to SAR inputs. The results demonstrate that the VAE’s reconstruction process adapts spatially to the noise level, effectively denoising the inputs while preserving structural details. This indicates that the VAE can embed SAR images into the same latent space as EO images without additional training, allowing SAR features to serve as conditioning inputs during the diffusion process. This ensures that pixel-wise correspondence between SAR and EO latent spaces is maintained throughout the generation process.

### 3.3. Training Strategy for the Diffusion Process

The diffusion process consists of two key stages: a forward process that progressively adds noise to the target EO feature, and a reverse process that Denoising U-Net  $\psi$  predicts and removes the added noise.

**Forward process.** Following the DDPMs [18] framework, noise is added to the target EO feature  $\mathbf{z}_y$  over a sequence of timesteps  $t \sim \mathcal{U}(T)$ , where  $\mathcal{U}$  is a uniform distribution and  $T$  is a total number of timesteps. Specifically, at each timestep  $t$ , a noisy version of the EO feature  $\mathbf{z}_y^t$  is generated by sampling:

$$\mathbf{z}_y^t = \sqrt{\bar{\alpha}_t} \mathbf{z}_y + \sqrt{1 - \bar{\alpha}_t} \epsilon, \epsilon \sim \mathcal{N}(\mathbf{0}, \mathbf{I}), \quad (1)$$

where  $\mathcal{N}$  is a Gaussian distribution,  $\epsilon \in \mathbb{R}^{h \times w \times C}$ , and  $\bar{\alpha}_t = \prod_{s=1}^t (1 - \beta_s)$  [18] determines the noise magnitude at each timestep  $t$ .

**Reverse process.**  $\psi$  learns the reverse process by predicting the added noise  $\epsilon$ , aligning with the pretrained LDM design. To leverage the pre-trained LDM’s text-to-image capability and provide a strong initialization, we use a fixed prompt,  $p = \text{“electro-optical image”}$ , as a stable conditioning signal. This guides the LDM to focus on EO-specific features by embedding the prompt via the CLIP [46] text encoder  $\mathcal{E}_{\text{text}}$  as  $\mathbf{z}_c = \mathcal{E}_{\text{text}}(p)$ , rather than using a null prompt.  $\psi$  takes as input the noisy EO feature  $\mathbf{z}_y^t$  and conditioned SAR feature  $\mathbf{z}_x$ , concatenated along the channel dimension, and is also fed with the timestep  $t$  and the text prompt embedding  $\mathbf{z}_c$ . Then, we have two output components: a predicted noise  $\hat{\epsilon}_t$  and a confidence map  $\hat{\mathbf{c}}_t \in \mathbb{R}^{h \times w \times 1}$  that contains the pixel-wise uncertainty of  $\hat{\epsilon}_t$ :

$$[\hat{\epsilon}_t \mid \hat{\mathbf{c}}_t] = \psi([\mathbf{z}_y^t \mid \mathbf{z}_x], \mathbf{z}_c, t), \quad (2)$$

where  $[\cdot \mid \cdot]$  indicates channel-wise concatenation. The confidence map  $\hat{\mathbf{c}}_t$  is further processed through a SoftPlus [10] operation to ensure all values remain non-negative.

**Confidence-guided diffusion (C-Diff) loss.** Seitzer *et al.* [53] proposed the  $\beta$ -NLL loss to capture aleatoric uncertainty for regression, classification and generative tasks. Inspired by the  $\beta$ -NLL loss [53, 65], we firstly adopt it into the training stage of diffusion process to enhance pixel-wise fidelity and to manage temporal inconsistencies between SAR and EO images. We apply the confidence output of  $\psi$  at each diffusion step to the  $\beta$ -NLL loss for stable SET, which is called C-Diff loss  $\mathcal{L}_{\text{C-Diff}}$ . That is,  $\mathcal{L}_{\text{C-Diff}}$  uses a learned confidence map  $\hat{\mathbf{c}}_t$  to adaptively weight the predicted noise  $\hat{\epsilon}_t$  pixel-wise.  $\mathcal{L}_{\text{C-Diff}}$  is designed to prioritize high-confidence areas while dewatering uncertain regions, thus improving robustness in regions with temporal misalignments (e.g., dynamic objects in SAR or EO images).  $\mathcal{L}_{\text{C-Diff}}$  optimizes  $\psi$  by combining a weighted pixel-wise reconstruction loss and a regularization term for the confidence map  $\hat{\mathbf{c}}_t$ :

$$\mathcal{L}_{\text{C-Diff}} = \left\| (\epsilon - \hat{\epsilon}_t) \odot \hat{\mathbf{c}}_t^\beta - \log \hat{\mathbf{c}}_t^\beta + \tau \right\|_2, \quad (3)$$

where  $\tau$  is a margin term ensuring non-negativity of the loss.  $\hat{\mathbf{c}}_t$  effectively acts as an adaptive weighting factor, allowing the model to focus more on well-aligned regions and reduce penalties in uncertain areas. The log term serves as a regularizer, preventing  $\hat{\mathbf{c}}_t$  from collapsing to zero. Empirically, we found that setting  $\beta = 1$  yields the best performance, while  $\beta = 0$  reduces  $\mathcal{L}_{\text{C-Diff}}$  to a standard  $\ell_2$  (MSE) loss, lacking adaptive weighting.  $\mathcal{L}_{\text{C-Diff}}$  allows C-DiffSET to produce EO outputs of high structural accuracy while mitigating artifacts and hallucinations that can arise in temporally inconsistent regions.

### 3.4. Inference Stage for EO Image Prediction

Given an unseen SAR image  $\mathbf{X}$ , we pass it through the VAE encoder  $\mathcal{E}_{\text{vae}}$  to obtain its SAR latent code  $\mathbf{z}_x = \mathcal{E}_{\text{vae}}(\mathbf{X})$ ,

which serves as the conditioning information for the reverse diffusion process. For inference, the Denoising U-Net  $\psi$  iteratively refines the noisy latent code  $\hat{\mathbf{z}}_y^T$ , to reconstruct the target EO latent code  $\mathbf{z}_y^0 = \mathbf{z}_y$  by denoising it back to the clean EO latent code through noise prediction  $\hat{\epsilon}_t$ . Starting from pure noise,  $\hat{\mathbf{z}}_y^T \sim \mathcal{N}(\mathbf{0}, \mathbf{I})$ ,  $\psi$  iteratively refines the EO latent code  $\hat{\mathbf{z}}_y^t$  by predicting the noise  $\hat{\epsilon}_t$  to be removed at each timestep  $t$  as:

$$[\hat{\epsilon}_t \mid \text{Dummy}] = \psi([\hat{\mathbf{z}}_y^t \mid \mathbf{z}_x], \mathbf{z}_c, t), \quad (4)$$

where Dummy indicates dummy confidence values. The predicted noise  $\hat{\epsilon}_t$  is then used to compute  $\hat{\mathbf{z}}_y^{t-1}$  in the reverse diffusion process, following the formulation in [18], which progressively denoises the EO latent code until it converges to the target EO latent code. The final EO latent code  $\hat{\mathbf{z}}_y^0$  is passed through the VAE decoder  $\mathcal{D}_{\text{vae}}$  to generate the reconstructed EO image  $\hat{\mathbf{Y}} = \mathcal{D}_{\text{vae}}(\hat{\mathbf{z}}_y^0)$ .

## 4. Experiment

### 4.1. Datasets

We evaluate our C-DiffSET framework on three publicly available SAR-to-EO datasets: QXS-SAROPT [19], SAR2Opt [83], and SpaceNet6 [56]. These datasets vary in satellite platforms, GSD [61], and SAR polarization modes, allowing us to assess the robustness and generalizability of our approach across diverse real-world scenarios. The SAR images in these publicly released datasets are provided as *magnitude-only* representation, containing real-valued intensity without phase information.

**QXS-SAROPT** [19]. The QXS-SAROPT dataset contains 20,000 SAR and EO image pairs captured by the Gaofen-3 satellite (SAR) and Google Earth (EO). The SAR images are acquired in a single-polarization mode. The EO images consist of RGB channels, covering various port cities. Each image patch measures  $256 \times 256$  pixels with an  $1\text{-m}$  GSD, focusing on complex maritime environments.

**SAR2Opt** [83]. The SAR2Opt dataset provides 2,076 SAR and EO image pairs obtained from the TerraSAR-X satellite (SAR) and Google Earth (EO). The SAR images are captured in a single-polarization mode. The corresponding EO images contain RGB channels and cover diverse Asian cities. Each patch measures  $600 \times 600$  pixels with an  $1\text{-m}$  GSD, making this dataset particularly useful for urban area analysis and infrastructure monitoring.

**SpaceNet6** [56]. The SpaceNet6 dataset offers SAR and EO image pairs captured by Capella Space (SAR) and Maxar WorldView-2 (EO) satellites. The SAR images are acquired with full-polarization, enabling detailed analysis of surface structures. The EO images include RGB and NIR bands, though only the RGB subset is used in our experiments. This dataset contains 3,401 SAR-EO image pairs,

with each patch size of  $900 \times 900$  pixels and a  $0.5\text{-m}$  GSD, focusing on urban landscapes and building detection tasks.

### 4.2. Experiment Details

All experiments were implemented using PyTorch [43] and conducted on a single NVIDIA A6000 GPU. Each model was fine-tuned for 50,000 iterations, with a 100-step warmup period. We employed the AdamW optimizer [37] with an initial learning rate of  $3 \times 10^{-5}$  and a weight decay of 0.01. A cosine-annealing scheduler [38] was used to progressively reduce the learning rate at each iteration. For the pretrained LDM, we utilized Stable Diffusion v2.1 [47, 63], and the text encoder was frozen as the CLIP-ViT-H/14 [23, 46] text encoder. For the latent features, we set the spatial resolution to  $h = H/8$  and  $w = W/8$ , and the channel dimension to  $C = 4$ . The training noise scheduler was based on DDPM [18] with a total of 1,000 steps. For inference, we employed an efficient DDIM [58] noise scheduler with total 50 inference steps to accelerate the generation process. We evaluated the performance of our framework using Fréchet Inception Distance (FID) [17], Learned Perceptual Image Patch Similarity (LPIPS) [80], Spatial Correlation Coefficient (SCC) [86], Structural Similarity Index (SSIM) [66], and Peak Signal-to-Noise Ratio (PSNR).

### 4.3. Experimental Results

For comparative analysis, we used official implementations for general image-to-image translation methods [24, 33, 70, 72, 77, 82, 87]. For LDM-based methods, including our C-DiffSET, it should be noted that we ensured fair comparison by initializing all models with the same Stable Diffusion v2.1 weights (VAE, U-Net). For SET-specific methods [28, 31, 73] (marked by †), where their official codes are often unavailable due to this specific field, we re-implemented each method according to their technical descriptions.

**Qualitative comparison.** As shown in Fig. 1 and Fig. 5, the GAN-based methods generally struggle with stability during training, leading to prominent artifacts in SET. The LDM-based methods, such as BBDM [33] and cBBDM [28], face challenges due to their reliance on direct diffusion from SAR input  $\mathbf{X}$  to EO output  $\mathbf{Y}$ . This setup makes them particularly susceptible to local spatial misalignments, producing blurred and incoherent results. DGDM [72] seeks to improve the initial stage of diffusion through a deterministic approach, employing a lightweight translation network to create a translated EO latent from SAR latent. However, the simplistic nature of this translation network fails to capture the intricate EO features, resulting in suboptimal initial latents for the diffusion process. Furthermore, ControlNet-based approaches [77, 82] keep the pretrained U-Net weights frozen and only introduce SAR conditions at the decoder stage, limiting their ability to fully integrate SAR structural information. This constraint results in





Figure 5. Visual comparison of SET results on the SpaceNet6 and SAR2Opt datasets. 1st rows: GAN-based (Pix2pix, CycleGAN, CFCA-SET, and StegoGAN) methods. 2nd rows: LDM-based (BBDM, ControlNet, Uni-ControlNet, DGDM, cBBDM, and C-DiffSET) methods.

weaker feature adaptation and reduced robustness to SAR-induced artifacts. In contrast, our C-DiffSET leverages pre-trained LDM as foundational model, effectively addressing alignment issues via a confidence-guided diffusion loss, leading to yield sharper and more structurally coherent EO images, and to outperform both GAN-based and diffusion-based baselines in visual fidelity.

**Quantitative evaluation.** In Table 1 and Table 2, the GAN-based methods benefit from the richer polarization diversity in SpaceNet6 dataset (4-channel full-polarization SAR data), yielding higher SSIM and SCC scores compared to 1-channel single-polarization datasets. However, for the other perceptual quality metrics such as FID and LPIPS, the GAN-based methods yield lower performance across datasets, indicating their inherent limitations in handling the SET task. The LDM-based methods, BBDM and cBBDM, also perform inadequately due to their direct diffusion setup from SAR to EO, which exacerbates the pixel-wise misalignment

problem and inflates LPIPS and FID scores. The DGDM incorporates a lightweight translator network to initialize the diffusion process, but its simplistic structure fails to encapsulate detailed EO features, resulting in lower PSNR and SSIM scores. In contrast, our C-DiffSET achieves superior performance across all metrics, enabled by the pretrained LDM and confidence-guided diffusion loss, which jointly tackle SAR-specific noise and alignment challenges. This adaptation allows C-DiffSET to attain the highest PSNR, SSIM, and SCC values, along with the lowest LPIPS and FID scores, highlighting its enhanced fidelity and perceptual quality in SET.

#### 4.4. Ablation Studies

**Impact of pretrained LDM and  $\mathcal{L}_{C-Diff}$ .** We ablate the contribution of the pretrained LDM and the confidence-guided diffusion loss  $\mathcal{L}_{C-Diff}$  for the SAR2Opt and SpaceNet6 datasets, and show the results in Table 3.



Types	Methods	Publications	SAR2Opt Dataset					SpaceNet6 Dataset				
			FID↓	LPIPS↓	SCC↑	SSIM↑	PSNR↑	FID↓	LPIPS↓	SCC↑	SSIM↑	PSNR↑
GANs	Pix2Pix [24]	CVPR 2017	196.87	0.426	0.0006	0.216	15.422	124.55	0.256	0.0102	0.522	19.357
	CycleGAN [87]	ICCV 2017	139.72	0.425	0.0022	0.224	14.931	114.81	0.274	0.0097	0.493	17.798
	SAR-SMTNet <sup>†</sup> [73]	TGRS 2023	160.87	0.479	0.0011	0.219	14.661	118.96	0.294	0.0103	0.483	17.032
	CFCA-SET <sup>†</sup> [31]	TGRS 2023	152.27	0.430	0.0009	0.223	15.183	164.78	0.279	0.0097	0.498	18.297
	StegoGAN [70]	CVPR 2024	144.54	0.398	0.0034	0.237	15.624	75.12	0.244	0.0106	0.516	18.958
LDMs	BBDM [33]	CVPR 2023	94.72	0.473	0.0005	0.234	15.131	81.86	0.302	0.0019	0.217	17.678
	ControlNet [77]	ICCV 2023	81.04	0.423	0.0005	0.216	14.461	106.59	0.392	0.0027	0.178	14.085
	Uni-ControlNet [82]	NeurIPS 2023	80.81	0.421	0.0004	0.215	14.384	91.14	0.321	0.0037	0.183	14.333
	DGDM [72]	ECCV 2024	156.12	0.541	0.0004	0.273	15.568	238.37	0.438	0.0015	0.253	17.124
	cBBDM <sup>†</sup> [28]	arXiv 2024	97.64	0.394	0.0022	0.285	16.591	72.77	0.243	0.0079	0.254	19.033
	<b>C-DiffSET (Ours)</b>	-	<b>77.81</b>	<b>0.346</b>	<b>0.0035</b>	<b>0.286</b>	<b>16.613</b>	<b>37.44</b>	<b>0.142</b>	<b>0.0151</b>	<b>0.567</b>	<b>21.022</b>

Table 1. Quantitative comparison of image-to-image translation methods and SET methods on SAR2Opt and SpaceNet6 datasets. **Red** indicate the best performance in each metric.

Types	Methods	QXS-SAROPT Dataset				
		FID↓	LPIPS↓	SCC↑	SSIM↑	PSNR↑
GANs	Pix2Pix [24]	196.89	0.454	0.0000	0.247	14.924
	CycleGAN [87]	195.38	0.455	0.0001	0.251	14.977
	SAR-SMTNet <sup>†</sup> [73]	117.69	0.435	0.0003	0.260	14.491
	CFCA-SET <sup>†</sup> [31]	79.06	0.406	0.0006	0.273	15.094
	StegoGAN [70]	85.60	0.391	0.0019	0.280	15.580
LDMs	BBDM [33]	65.15	0.522	0.0004	0.238	13.946
	ControlNet [77]	22.39	0.434	0.0001	0.257	14.062
	Uni-ControlNet [82]	22.48	0.437	0.0002	0.257	13.985
	DGDM [72]	147.23	0.634	0.0001	0.288	11.564
	cBBDM <sup>†</sup> [28]	69.47	0.420	0.0023	0.304	16.248
	<b>C-DiffSET (Ours)</b>	<b>18.15</b>	<b>0.293</b>	<b>0.0108</b>	<b>0.372</b>	<b>18.077</b>

Table 2. Quantitative comparison of image-to-image translation methods and SET methods on the QXS-SAROPT dataset.

The pretrained LDM provides strong initialization for EO generation, improving the baseline PSNR and SSIM scores when compared to training from scratch. Even though the LDM-based methods and our C-DiffSET utilize the same pretrained LDM weights, our C-DiffSET outperformed the others by embedding conditioned SAR and target EO images into the shared latent space, leading to stable convergence. Furthermore,  $\mathcal{L}_{C-Diff}$  helps enhancing the SSIM and PSNR metrics and lowering LPIPS and FID values, thus improving both perceptual fidelity and structural consistency. Fig. 6 shows confidence maps generated on the training dataset at timestep  $t = T/2$  (midpoint of the denoising process), highlighting the areas of temporal discrepancy in SAR-EO pairs. This loss enables the U-Net  $\psi$  to down-weight uncertain regions where objects are temporally misaligned across modalities, thereby reducing artifacts and ensuring coherent EO outputs. Further results and detailed analysis can be found in the *Supplemental Material*.

#### 4.5. Limitations

**Scalability across diverse satellites.** The VAE in C-DiffSET is designed for 3-channel inputs, matching typical RGB images. This limits its direct application to datasets with more channels (e.g., RGB+NIR or multispectral data). An extension to supporting such inputs would require further exploration and tuning for effective adaptation.

Pretrained LDM	Loss function	SAR2Opt / SpaceNet6 Dataset				
		FID↓	LPIPS↓	SCC↑	SSIM↑	PSNR↑
✓	MSE	98.98 / 60.26	0.39 / 0.23	0.001 / 0.011	0.26 / 0.43	15.82 / 18.16
	MSE	78.14 / 40.62	0.36 / 0.16	0.003 / 0.014	0.28 / 0.52	16.46 / 20.29
✓	C-Diff	<b>77.81 / 37.44</b>	<b>0.34 / 0.14</b>	<b>0.004 / 0.015</b>	<b>0.29 / 0.57</b>	<b>16.61 / 21.02</b>

Table 3. Ablation studies on the SAR2Opt and SpaceNet6 dataset evaluating the impact of pretrained LDM and confidence-guided diffusion (C-Diff) loss.

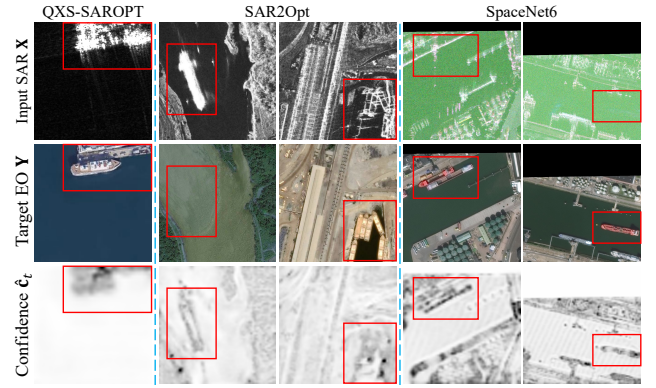


Figure 6. Confidence maps generated by C-DiffSET at timestep  $t = T/2$  on SAR-EO paired datasets: QXS-SAROPT, SAR2Opt, and SpaceNet6. Each row illustrates the input SAR image  $X$ , the target EO image  $Y$ , and the corresponding confidence map  $\hat{c}_t$ .

## 5. Conclusion

In this work, we propose C-DiffSET, a novel framework that addresses key challenges in SAR-to-EO image translation. To the best of our knowledge, this is the first method to fully leverage LDM for SET tasks, mitigating issues caused by the limited availability of paired datasets. We introduce a C-Diff loss to handle temporal discrepancy between SAR and EO acquisitions, ensuring pixel-wise fidelity by adaptively suppressing artifacts and hallucinations. C-DiffSET achieves SOTA performance across datasets with varying GSD, demonstrating its effectiveness in real-world scenarios. Our framework provides a scalable foundation for future SET research and can be extended to other remote sensing applications and modalities.

## A. Additional Discussions on Results

### A.1. Additional Qualitative Comparisons

Fig. 16, Fig. 12, Fig. 13, Fig. 14, Fig. 15, Fig. 17, Fig. 18, Fig. 19, and Fig. 20 provide additional qualitative comparisons of SAR-to-EO image translation results on the QXS-SAROPT [50], SAR2Opt [83], and SpaceNet6 [56] datasets. The GAN-based methods, including Pix2Pix [24] and CycleGAN [87], exhibit severe artifacts due to the inherent instability of the training process within the GAN frameworks. Although CFCA-SET [31] and StegoGAN [70] mitigate some of these artifacts, they still produce visually inconsistent results, often failing to preserve fine-grained structural details. Among the LDM-based approaches, BBDM [33] and cBBDM [28] generate smoother outputs and struggle with oversimplified textures and lack of structural alignment due to their direct diffusion process. DGDM [72] relies on an initial translator network to generate SAR-to-EO latents; however, the simplicity of this translator leads to poorly initialized latents, resulting in entirely unrealistic outputs. ControlNet-based approaches [77, 82] exhibit similar limitations, as they keep the pretrained U-Net weights frozen and inject SAR conditions only in the decoder stage, failing to fully propagate the structural information of SAR throughout the denoising process. In contrast, our proposed C-DiffSET effectively addresses these limitations, producing visually coherent and structurally accurate EO images that are closely aligned with the target EO images.

### A.2. Analysis of Domain Gap and Upper Bound Performance

In Fig. 4 of the main paper, we evaluate the reconstruction quality of the VAE encoder  $\mathcal{E}_{\text{vae}}$  and decoder  $\mathcal{D}_{\text{vae}}$  from the LDM by visualizing their outputs for target EO images and SAR images with varying levels of speckle noise.

**Embedding into a shared latent space.** In Fig. 7, additional VAE reconstruction results demonstrate that SAR and EO images are embedded into the same latent space. Notably, VAE-reconstructed SAR images preserve structural information while reducing speckle noise, enhancing their suitability as conditioning inputs for SET task.

**Domain gap analysis.** Fig. 7, Table 4, Table 5, and Table 6 show that the VAE, trained on natural image datasets, effectively reconstructs the RGB bands of EO images. This indicates that the domain gap between natural images and EO imagery in the RGB spectrum is relatively small, enabling the pretrained LDM to generalize well to EO data. This observation further supports our approach of leveraging a large-scale pretrained diffusion model for the SET task.

**Upper bound comparison.** Our proposed C-DiffSET framework, built on the LDM architecture, predicts the target EO features  $\mathbf{z}_y = \mathcal{E}_{\text{vae}}(\mathbf{Y})$  embedded in the latent space

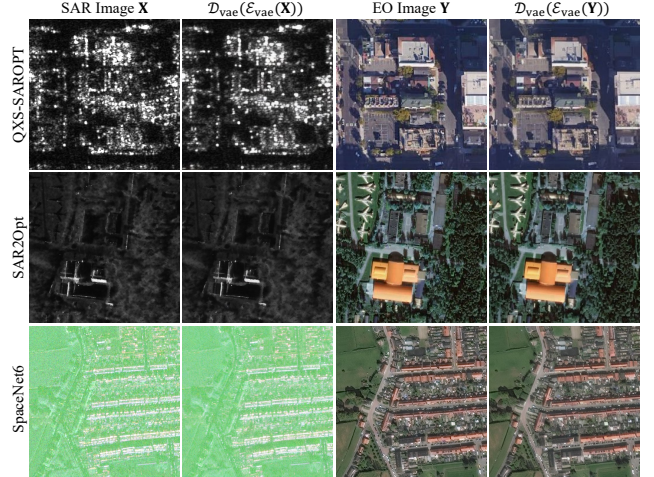


Figure 7. Results of applying the VAE encoder and decoder from LDM to EO and SAR images. These results suggest that the LDM VAE facilitates a shared latent representation between SAR and EO domains, supporting robust cross-domain image translation.

Methods	SpaceNet6 Test Dataset				
	FID↓	LPIPS↓	SCC↑	SSIM↑	PSNR↑
C-DiffSET (Ours)	85.77	0.132	0.0210	0.546	21.498
$\mathcal{D}_{\text{vae}}(\mathcal{E}_{\text{vae}}(\mathbf{Y}))$	17.64	0.047	0.1417	0.800	28.543

Table 4. Comparison of C-DiffSET performance with the VAE upper bound on the SpaceNet6 dataset. The upper bound represents the maximum achievable quality defined by the VAE-decoded target EO features.

Methods	SAR2Opt Test Dataset				
	FID↓	LPIPS↓	SCC↑	SSIM↑	PSNR↑
C-DiffSET (Ours)	77.81	0.346	0.0035	0.286	16.613
$\mathcal{D}_{\text{vae}}(\mathcal{E}_{\text{vae}}(\mathbf{Y}))$	28.99	0.095	0.1583	0.667	25.678

Table 5. Comparison of C-DiffSET performance with the VAE upper bound on the SAR2Opt dataset.

Methods	QXS-SAROPT Test Dataset				
	FID↓	LPIPS↓	SCC↑	SSIM↑	PSNR↑
C-DiffSET (Ours)	18.15	0.293	0.0108	0.372	18.077
$\mathcal{D}_{\text{vae}}(\mathcal{E}_{\text{vae}}(\mathbf{Y}))$	9.18	0.064	0.2597	0.794	29.497

Table 6. Comparison of C-DiffSET performance with the VAE upper bound on the QXS-SAROPT dataset.

through the VAE encoder. The VAE-decoded reconstruction of the target EO feature,  $\mathcal{D}_{\text{vae}}(\mathbf{z}_y) = \mathcal{D}_{\text{vae}}(\mathcal{E}_{\text{vae}}(\mathbf{Y}))$ , serves as an upper bound for our C-DiffSET, representing the maximum achievable quality given the pretrained LDM. Table 4, Table 5, and Table 6 quantitatively compare the performance of C-DiffSET against this upper bound. Although our framework achieves strong results, particularly in perceptual metrics such as LPIPS and FID, the gap to the upper bound highlights the inherent challenges in SAR-to-EO

Types	Methods	Params. (M)	FLOPs (G)	Memory (MB)	Time (s)
GANs	Pix2Pix [24]	54.41	24.22	464.12	0.06
	CycleGAN [87]	7.84	140.43	398.38	0.08
	SAR-SMTNet [73]	2.15	615.40	2626.98	0.22
	CFCA-SET [31]	26.80	98.98	431.86	0.10
	StegoGAN [70]	13.15	227.49	461.14	0.11
LDMs	BBDM [33]	949.56	2122.44	6147.88	3.13
	ControlNet [77]	1312.72	2231.03	7567.83	4.50
	Uni-ControlNet [82]	1519.18	2295.20	8382.00	4.95
	DGDM [72]	959.03	2161.25	6184.45	1.47
	cBBDM [28]	949.58	2122.49	6147.93	3.15
	<b>C-DiffSET</b>	949.58	2122.49	6148.09	3.27

Table 7. Comparative analysis of C-DiffSET with other methods by parameters, FLOPs, memory usage, and inference time.

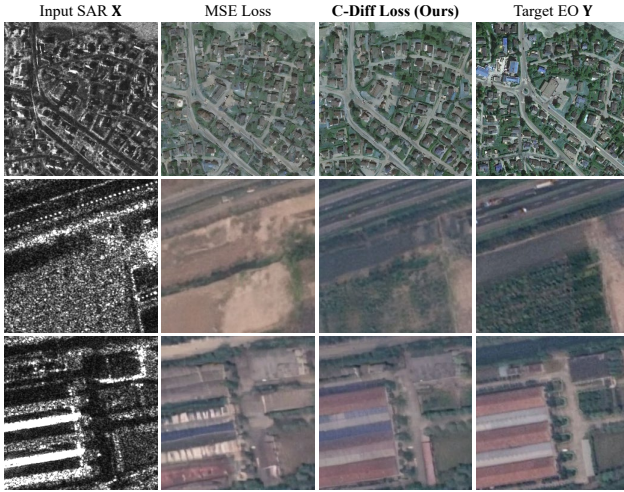


Figure 8. Visual comparison of SET results with and without C-Diff loss. The MSE loss corresponds to  $\beta = 0$ , indicating no confidence weighting.

Pretrained LDM	Loss function	QXS-SAROPT Dataset				
		FID↓	LPIPS↓	SCC↑	SSIM↑	PSNR↑
✓	MSE	29.04	0.407	0.0006	0.279	14.647
✓	MSE	19.99	0.297	0.0094	0.364	17.736
✓	C-Diff	<b>18.15</b>	<b>0.293</b>	<b>0.0108</b>	<b>0.372</b>	<b>18.077</b>

Table 8. Ablation studies on the QXS-SAROPT dataset evaluating the impact of pretrained LDM and confidence-guided diffusion (C-Diff) loss.

Text Prompt	SpaceNet6 Dataset				
	FID↓	LPIPS↓	SCC↑	SSIM↑	PSNR↑
“ ” (Null text, $\emptyset$ )	79.01	0.351	0.0027	0.273	16.237
“Electro-Optical Image”	<b>77.81</b>	<b>0.346</b>	<b>0.0035</b>	<b>0.286</b>	<b>16.613</b>

Table 9. Ablation studies on the text prompts.

translation, including noise, misalignment, and the structural complexity of SAR data. This analysis underscores the potential for future research to bridge this gap, pushing SET closer to the theoretical upper limit.

### A.3. Computational Complexity

We compare the number of parameters, FLOPs, memory usage, and inference time for  $512 \times 512$  images in Table 7. As noted, the LDM-based methods are more complex than the GAN-based ones. The time-performance trade-off is in Fig. 9.

### A.4. Progressive Denoising Visualization

Fig. 11 illustrates the progression of generated images across different inference timesteps during the reverse denoising process. Out of the total  $T_{\text{test}} = 50$  inference steps, we select 11 representative timesteps to visualize the progressive refinement of the output. Using the DDIM [58] noise scheduler, denoising is performed over 50 steps, with timesteps chosen from the range  $[1, T]$  to balance sampling efficiency and performance. At earlier timesteps (e.g.,  $t = 981$ ), the images exhibit significant noise, reflecting the initial latent representation. As the process progresses to later timesteps (e.g.,  $t = 1$ ), the generated images become increasingly coherent, closely resembling the target EO images.

## B. Further Ablation Studies

### B.1. Impact of Pretrained LDM and C-Diff Loss

We provide in Table 8 further experiments on additional dataset to validate  $\mathcal{L}_{\text{C-Diff}}$ . Moreover, Fig. 8 presents visual comparisons of SET results under different loss functions, demonstrating the impact of  $\mathcal{L}_{\text{C-Diff}}$  on structural consistency and perceptual quality.

### B.2. Effect of Text Prompts

We provide additional ablation studies on the text prompt in Table 9. Since our datasets do not include text annotations, we use a generic prompt (fixed for all samples), with Stable Diffusion v2.1’s classifier-free guidance rather than a null prompt  $\emptyset$ .

### B.3. Effect of Total Inference Steps

In Fig. 9 and Fig. 10, we justify the selection of  $T_{\text{test}} = 50$  inference steps in our experiments. While setting the total inference steps to match the training steps ( $T = 1,000$ ) ensures high performance, it incurs prohibitive inference times. To balance performance and efficiency, we evaluate the tradeoff between inference time and metric performance by varying the DDIM noise scheduler’s inference steps. For computational feasibility, experiments are conducted on the first 50 samples of the SpaceNet6 dataset. The results indicate significant performance gains for lower step counts ( $T_{\text{test}} = 1$  to  $T_{\text{test}} = 50$ ), but diminishing returns beyond 50 steps, with negligible improvements in metrics such as FID, LPIPS, and PSNR. Based on this analysis, we select a total of 50 inference steps as the optimal trade-off, achieving



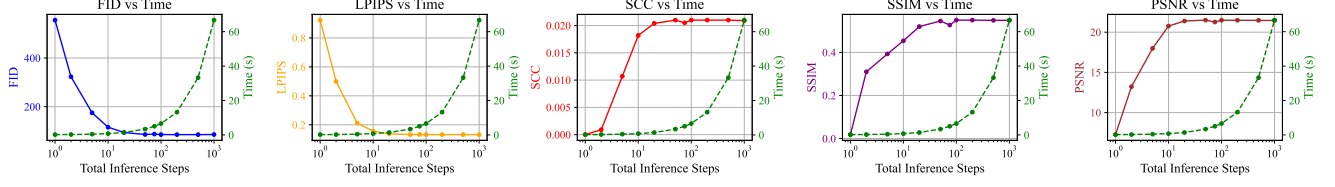


Figure 9. Impact of total inference steps on performance metrics (FID, LPIPS, SCC, SSIM, and PSNR) and inference time.



Figure 10. Visualization of C-DiffSET results across varying numbers of total inference steps.

high-quality outputs within practical inference times (3.376 seconds per  $512 \times 512$  image).

### C. Additional Experimental Details

Since SAR features were incorporated as additional inputs to the U-Net  $\psi$ , the weights of the  $\psi$ 's first convolutional layer were initialized by repeating the original weights across the SAR channels. Additionally, the confidence map was initialized to 1 to ensure stable optimization, starting from the standard  $\ell_2$  loss, and  $\tau = \log 2\pi$  [53] was applied. For the QXS-SAROPT dataset, we used the provided original  $256 \times 256$ -sized patches without modification, with a batch size of 64. For the SAR2Opt and SpaceNet6 datasets, we performed random cropping to  $512 \times 512$ -sized patches and set the batch size to 16. Data augmentation techniques, including random horizontal and vertical flips and random rotations (multiples of 90 degrees), were applied during training to improve generalization. To prevent overfitting and mitigate pretrained weight forgetting, we used a small initial learning rate of  $3 \times 10^{-5}$ . To ensure reproducibility, a random seed of 2,025 was fixed for all experiments. Data was split with 80% used for training and 20% for testing across all experiments.

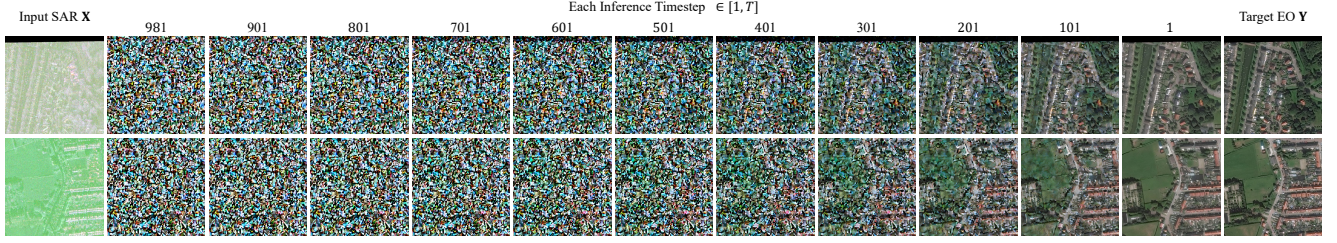


Figure 11. Visualization of C-DiffSET results across inference timesteps on the SpaceNet6 dataset with a total of 50 inference steps. Each column corresponds to an inference step, starting with substantial noise at  $t = 981$  and progressively refining the output to match the target EO image at  $t = 1$ .

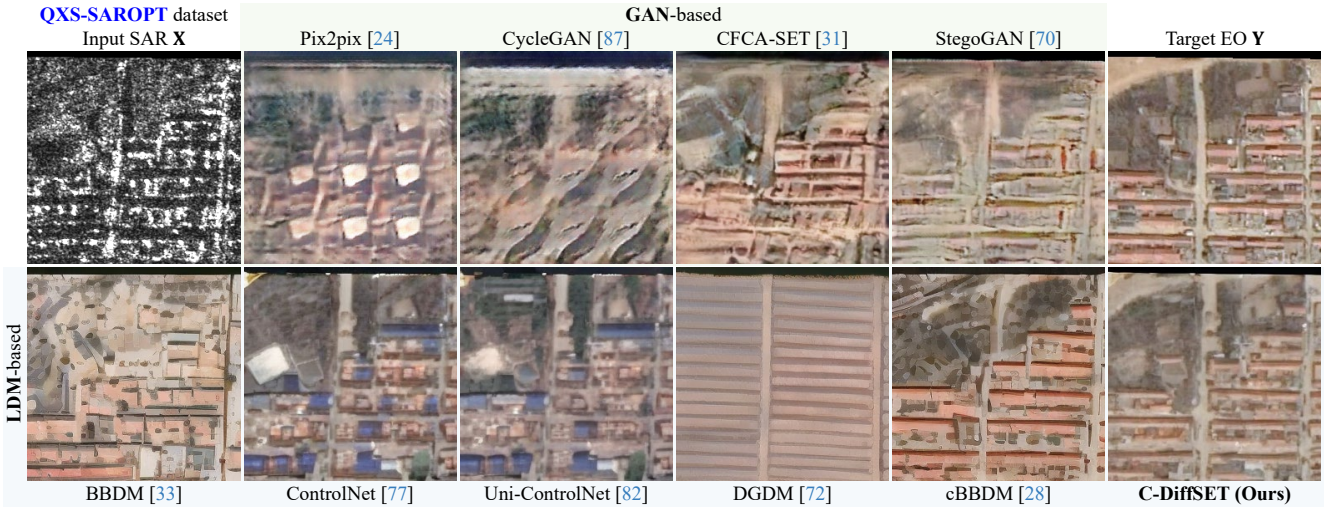


Figure 12. Visual comparison of SET results on the QXS-SAROPT dataset. 1st rows: GAN-based (Pix2pix, CycleGAN, CFCA-SET, and StegoGAN) methods. 2nd rows: LDM-based (BBDM, ControlNet, Uni-ControlNet, DGDM, cBBDM, and C-DiffSET) methods.

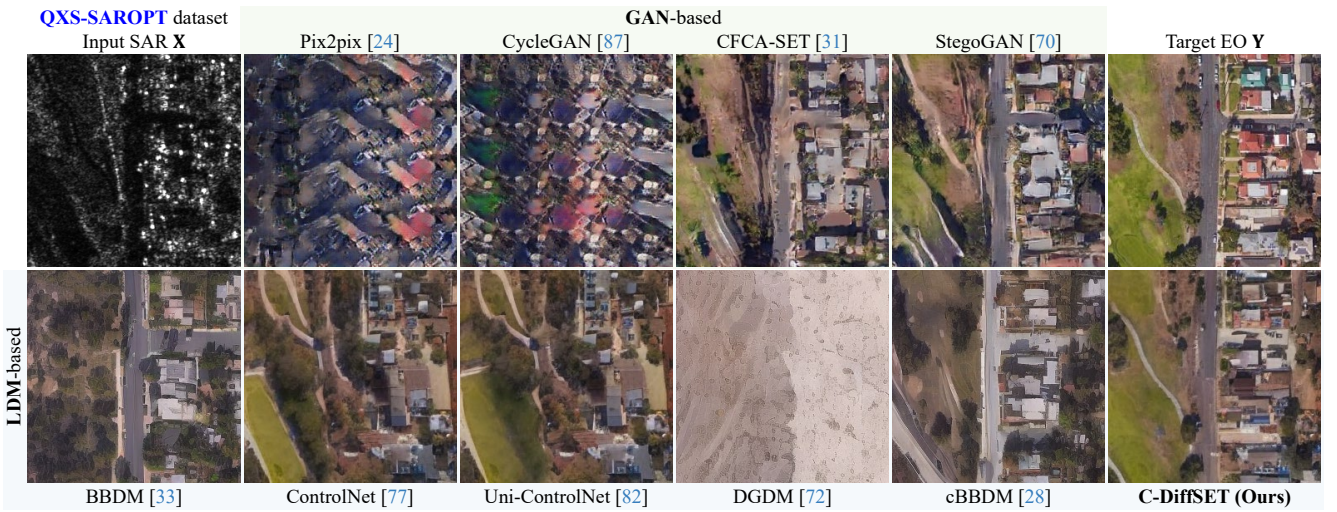


Figure 13. Visual comparison of SET results on the QXS-SAROPT dataset. 1st rows: GAN-based (Pix2pix, CycleGAN, CFCA-SET, and StegoGAN) methods. 2nd rows: LDM-based (BBDM, ControlNet, Uni-ControlNet, DGDM, cBBDM, and C-DiffSET) methods.



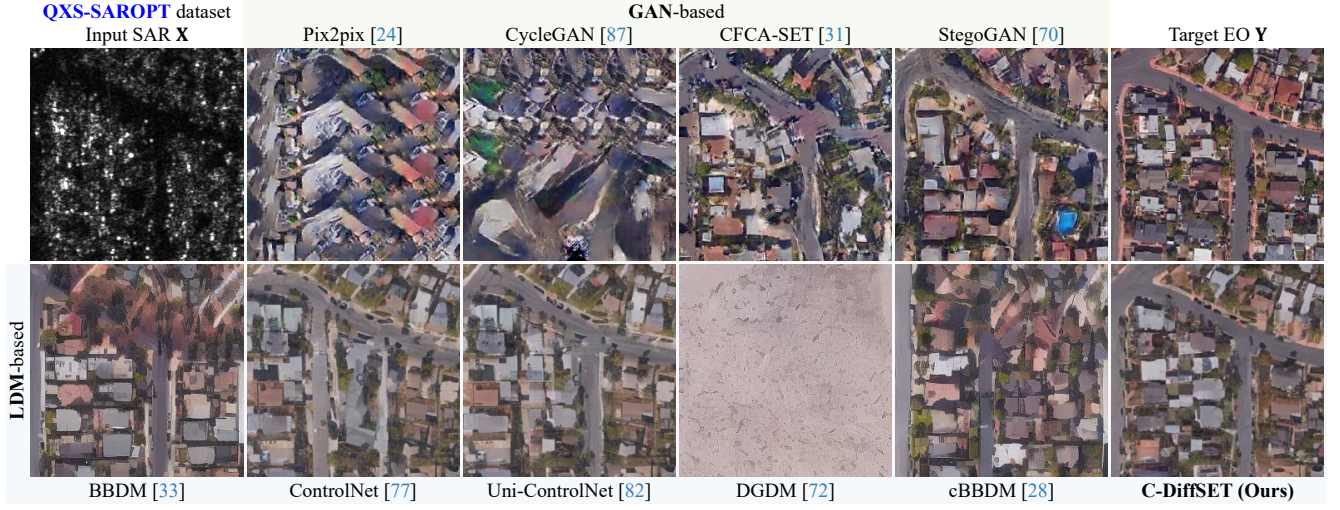


Figure 14. Visual comparison of SET results on the QXS-SAROPT dataset. 1st rows: GAN-based (Pix2pix, CycleGAN, CFCA-SET, and StegoGAN) methods. 2nd rows: LDM-based (BBDM, ControlNet, Uni-ControlNet, DGDM, cBBDM, and C-DiffSET) methods.

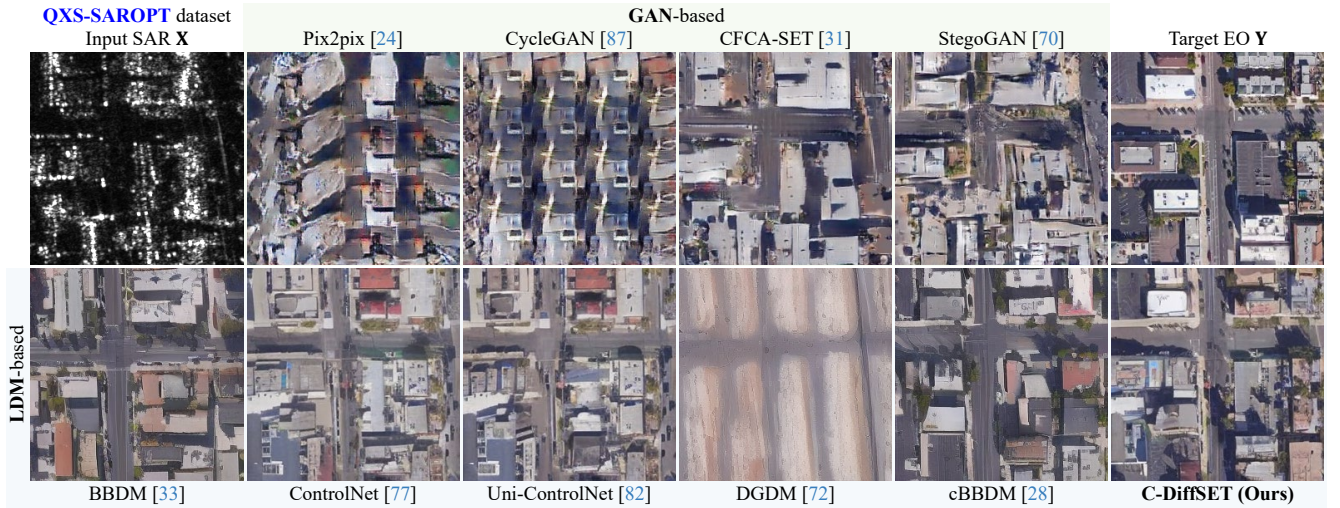


Figure 15. Visual comparison of SET results on the QXS-SAROPT dataset. 1st rows: GAN-based (Pix2pix, CycleGAN, CFCA-SET, and StegoGAN) methods. 2nd rows: LDM-based (BBDM, ControlNet, Uni-ControlNet, DGDM, cBBDM, and C-DiffSET) methods.



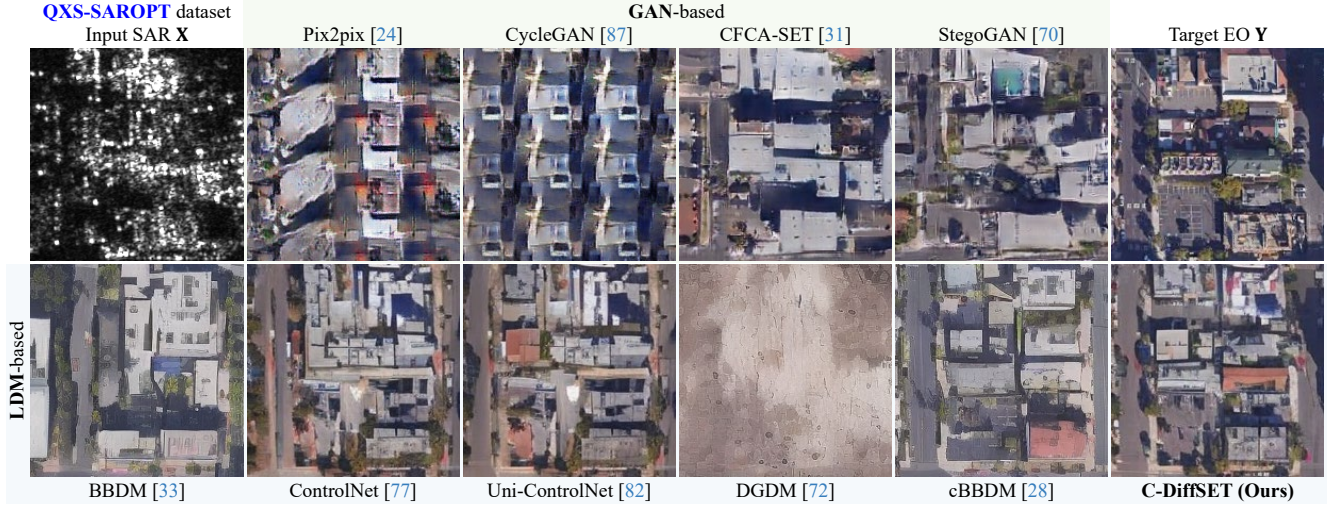


Figure 16. Visual comparison of SET results on the QXS-SAROPT dataset. 1st rows: GAN-based (Pix2pix, CycleGAN, CFCA-SET, and StegoGAN) methods. 2nd rows: LDM-based (BBDM, ControlNet, Uni-ControlNet, DGDM, cBBDM, and C-DiffSET) methods.

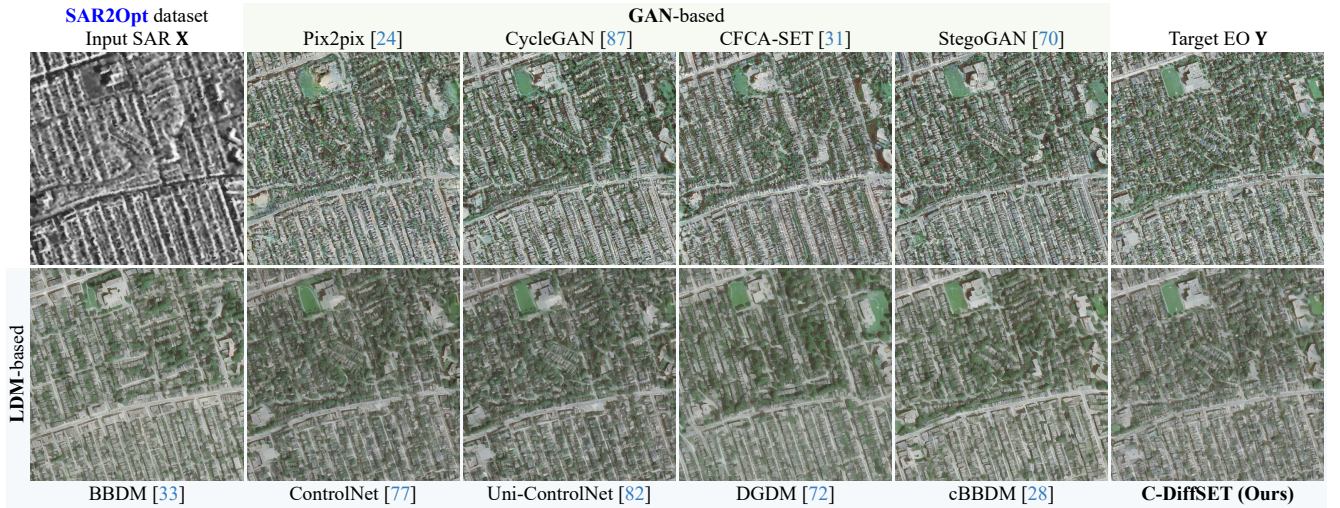


Figure 17. Visual comparison of SET results on the SAR2Opt dataset. 1st rows: GAN-based (Pix2pix, CycleGAN, CFCA-SET, and StegoGAN) methods. 2nd rows: LDM-based (BBDM, ControlNet, Uni-ControlNet, DGDM, cBBDM, and C-DiffSET) methods.



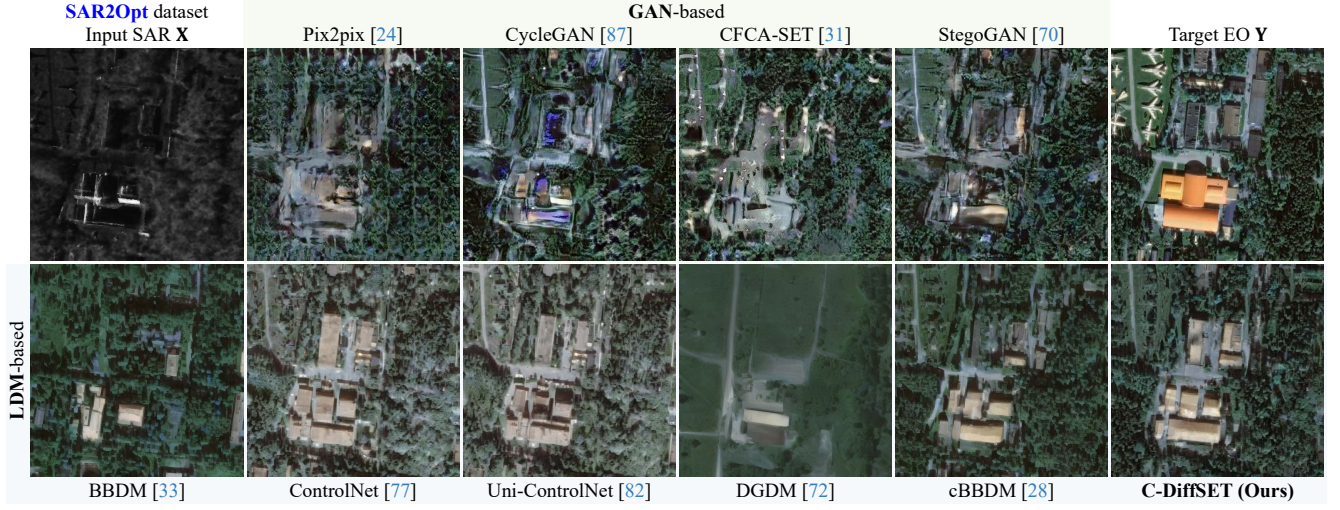


Figure 18. Visual comparison of SET results on the SAR2Opt dataset. 1st rows: GAN-based (Pix2pix, CycleGAN, CFCA-SET, and StegoGAN) methods. 2nd rows: LDM-based (BBDM, ControlNet, Uni-ControlNet, DGDM, cBBDM, and C-DiffSET) methods.

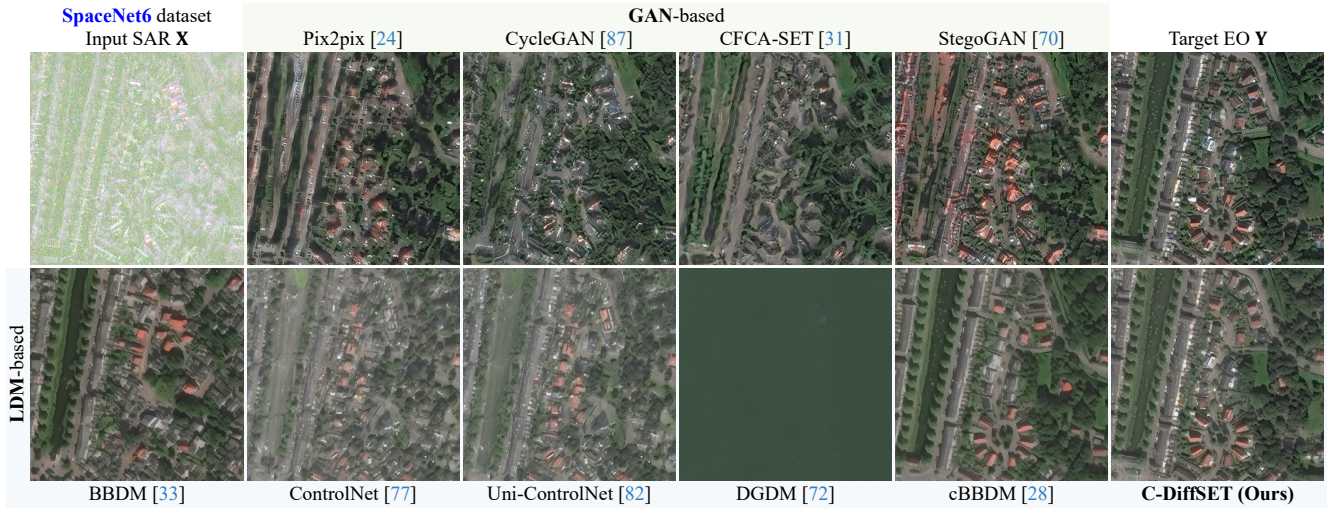


Figure 19. Visual comparison of SET results on the SpaceNet6 dataset. 1st rows: GAN-based (Pix2pix, CycleGAN, CFCA-SET, and StegoGAN) methods. 2nd rows: LDM-based (BBDM, ControlNet, Uni-ControlNet, DGDM, cBBDM, and C-DiffSET) methods.

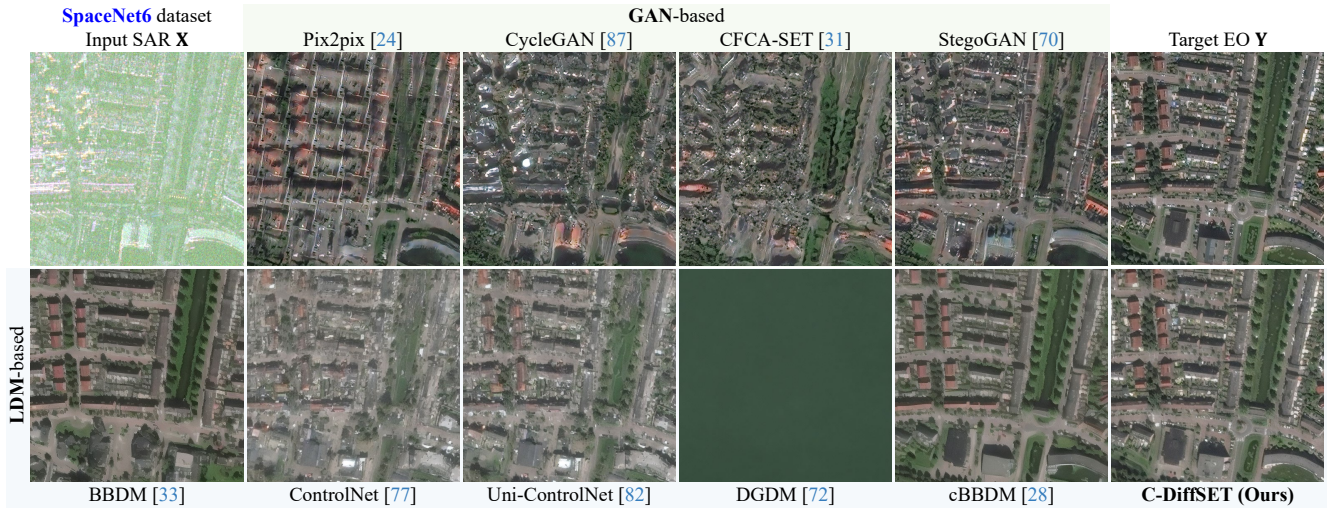


Figure 20. Visual comparison of SET results on the SpaceNet6 dataset. 1st rows: GAN-based (Pix2pix, CycleGAN, CFCA-SET, and StegoGAN) methods. 2nd rows: LDM-based (BBDM, ControlNet, Uni-ControlNet, DGDM, cBBDM, and C-DiffSET) methods.



## References

- [1] Kyungjune Baek, Yunje Choi, Youngjung Uh, Jaejun Yoo, and Hyunjung Shim. Rethinking the truly unsupervised image-to-image translation. In *Proceedings of the IEEE/CVF international conference on computer vision*, pages 14154–14163, 2021. 3
- [2] Xinyu Bai and Feng Xu. Sar to optical image translation with color supervised diffusion model. In *IGARSS 2024-2024 IEEE International Geoscience and Remote Sensing Symposium*, pages 963–966. IEEE, 2024. 3
- [3] Xinyu Bai, Xinyang Pu, and Feng Xu. Conditional diffusion for sar to optical image translation. *IEEE Geoscience and Remote Sensing Letters*, 2023. 3
- [4] Brian Brisco, Masoud Mahdianpari, and Fariba Mohammadimanesh. Hybrid compact polarimetric sar for environmental monitoring with the radarsat constellation mission. *Remote Sensing*, 12(20):3283, 2020. 2
- [5] Armando Cabrera, Miriam Cha, Prafull Sharma, and Michael Newey. Sar-to-eo image translation with multi-conditional adversarial networks. In *2021 55th Asilomar Conference on Signals, Systems, and Computers*, pages 1710–1714. IEEE, 2021. 3
- [6] Runfa Chen, Wenbing Huang, Binghui Huang, Fuchun Sun, and Bin Fang. Reusing discriminators for encoding: Towards unsupervised image-to-image translation. In *Proceedings of the IEEE/CVF conference on computer vision and pattern recognition*, pages 8168–8177, 2020. 3
- [7] Yunje Choi, Minje Choi, Munyoung Kim, Jung-Woo Ha, Sunghun Kim, and Jaegul Choo. Stargan: Unified generative adversarial networks for multi-domain image-to-image translation. In *Proceedings of the IEEE conference on computer vision and pattern recognition*, pages 8789–8797, 2018. 3
- [8] Mihai Datcu, Zhongling Huang, Andrei Anghel, Juanping Zhao, and Remus Căcovăanu. Explainable, physics-aware, trustworthy artificial intelligence: A paradigm shift for synthetic aperture radar. *IEEE Geoscience and Remote Sensing Magazine*, 11(1):8–25, 2023. 2, 3
- [9] Kento Doi, Ken Sakurada, Masaki Onishi, and Akira Iwasaki. Gan-based sar-to-optical image translation with region information. In *IGARSS 2020-2020 IEEE International Geoscience and Remote Sensing Symposium*, pages 2069–2072. IEEE, 2020. 3
- [10] Charles Dugas, Yoshua Bengio, François Bélisle, Claude Nadeau, and René Garcia. Incorporating second-order functional knowledge for better option pricing. *Advances in neural information processing systems*, 13, 2000. 5
- [11] Patrick Esser, Smith Kulal, Andreas Blattmann, Rahim Entezari, Jonas Müller, Harry Saini, Yam Levi, Dominik Lorenz, Axel Sauer, Frederic Boesel, et al. Scaling rectified flow transformers for high-resolution image synthesis. In *Forty-first International Conference on Machine Learning*, 2024. 2, 4
- [12] Jianhao Gao, Qiangqiang Yuan, Jie Li, Hai Zhang, and Xin Su. Cloud removal with fusion of high resolution optical and sar images using generative adversarial networks. *Remote Sensing*, 12(1):191, 2020. 2
- [13] Joseph W Goodman. Some fundamental properties of speckle. *JOSA*, 66(11):1145–1150, 1976. 2, 3
- [14] Austen Groener, Gary Chern, and Mark Pritt. A comparison of deep learning object detection models for satellite imagery. In *2019 IEEE applied imagery pattern recognition workshop (AIPR)*, pages 1–10. IEEE, 2019. 2
- [15] Zhe Guo, Jiayi Liu, Qinglin Cai, Zhibo Zhang, and Shaohui Mei. Learning sar-to-optical image translation via diffusion models with color memory. *IEEE Journal of Selected Topics in Applied Earth Observations and Remote Sensing*, 2024. 2, 3
- [16] Jing He, Haodong Li, Wei Yin, Yixun Liang, Leheng Li, Kaiqiang Zhou, Hongbo Liu, Bingbing Liu, and Ying-Cong Chen. Lotus: Diffusion-based visual foundation model for high-quality dense prediction. *arXiv preprint arXiv:2409.18124*, 2024. 4
- [17] Martin Heusel, Hubert Ramsauer, Thomas Unterthiner, Bernhard Nessler, and Sepp Hochreiter. Gans trained by a two time-scale update rule converge to a local nash equilibrium. *Advances in neural information processing systems*, 30, 2017. 6
- [18] Jonathan Ho, Ajay Jain, and Pieter Abbeel. Denoising diffusion probabilistic models. *Advances in neural information processing systems*, 33:6840–6851, 2020. 3, 5, 6
- [19] Meiyu Huang, Yao Xu, Lixin Qian, Weili Shi, Yaqin Zhang, Wei Bao, Nan Wang, Xuejiao Liu, and Xueshuang Xiang. The qxs-saropt dataset for deep learning in sar-optical data fusion. *arXiv preprint arXiv:2103.08259*, 2021. 3, 6
- [20] Xun Huang, Ming-Yu Liu, Serge Belongie, and Jan Kautz. Multimodal unsupervised image-to-image translation. In *Proceedings of the European conference on computer vision (ECCV)*, pages 172–189, 2018. 3
- [21] Zhongling Huang, Mihai Datcu, Zongxu Pan, and Bin Lei. A hybrid and explainable deep learning framework for sar images. In *IGARSS 2020-2020 IEEE International Geoscience and Remote Sensing Symposium*, pages 1727–1730. IEEE, 2020. 3
- [22] Satoshi Iizuka, Edgar Simo-Serra, and Hiroshi Ishikawa. Globally and locally consistent image completion. *ACM Transactions on Graphics (ToG)*, 36(4):1–14, 2017. 3
- [23] Gabriel Ilharco, Mitchell Wortsman, Nicholas Carlini, Rohan Taori, Achal Dave, Vaishaal Shankar, Hongseok Namkoong, John Miller, Hannaneh Hajishirzi, Ali Farhadi, and Ludwig Schmidt. Open clip, 2021. 6
- [24] Phillip Isola, Jun-Yan Zhu, Tinghui Zhou, and Alexei A Efros. Image-to-image translation with conditional adversarial networks. In *Proceedings of the IEEE conference on computer vision and pattern recognition*, pages 1125–1134, 2017. 3, 6, 8, 9, 10
- [25] Guang Ji, Zhaohui Wang, Lifan Zhou, Yu Xia, Shan Zhong, and Shengrong Gong. Sar image colorization using multidomain cycle-consistency generative adversarial network. *IEEE Geoscience and Remote Sensing Letters*, 18(2):296–300, 2020. 2, 3
- [26] Bingxin Ke, Anton Obukhov, Shengyu Huang, Nando Metzger, Rodrigo Caye Daudt, and Konrad Schindler. Repurposing diffusion-based image generators for monocular depth

- estimation. In *Proceedings of the IEEE/CVF Conference on Computer Vision and Pattern Recognition*, pages 9492–9502, 2024. 4
- [27] Soohyun Kim, Jongbeom Baek, Jihye Park, Gyeongnyeon Kim, and Seungryong Kim. Instaformer: Instance-aware image-to-image translation with transformer. In *Proceedings of the IEEE/CVF Conference on Computer Vision and Pattern Recognition*, pages 18321–18331, 2022. 3
- [28] Seon-Hoon Kim and Dae-won Chung. Conditional brownian bridge diffusion model for vhr sar to optical image translation. *arXiv preprint arXiv:2408.07947*, 2024. 2, 3, 6, 8, 9, 10
- [29] Diederik P Kingma. Auto-encoding variational bayes. *arXiv preprint arXiv:1312.6114*, 2013. 2
- [30] Yingying Kong, Siyuan Liu, and Xiangyang Peng. Multi-scale translation method from sar to optical remote sensing images based on conditional generative adversarial network. *International Journal of Remote Sensing*, 43(8):2837–2860, 2022. 3
- [31] Jaehyup Lee, Hyebin Cho, Doochun Seo, Hyun-Ho Kim, Jaehoon Jeong, and Munchurl Kim. Cfca-set: Coarse-to-fine context-aware sar-to-eo translation with auxiliary learning of sar-to-nir translation. *IEEE Transactions on Geoscience and Remote Sensing*, 2023. 2, 3, 6, 8, 9, 10
- [32] Jaehyup Lee, Hyun-Ho Kim, Doochun Seo, and Munchurl Kim. Segmentation-guided context learning using eo object labels for stable sar-to-eo translation. *IEEE Geoscience and Remote Sensing Letters*, 2023. 2, 3
- [33] Bo Li, Kaitao Xue, Bin Liu, and Yu-Kun Lai. Bbdlm: Image-to-image translation with brownian bridge diffusion models. In *Proceedings of the IEEE/CVF conference on computer vision and pattern recognition*, pages 1952–1961, 2023. 3, 6, 8, 9, 10
- [34] Xinghua Li, Zhengshun Du, Yanyuan Huang, and Zhenyu Tan. A deep translation (gan) based change detection network for optical and sar remote sensing images. *ISPRS Journal of Photogrammetry and Remote Sensing*, 179:14–34, 2021. 3
- [35] Yahui Liu, Enver Sangineto, Yajing Chen, Linchao Bao, Haoxian Zhang, Nicu Sebe, Bruno Lepri, Wei Wang, and Marco De Nadai. Smoothing the disentangled latent style space for unsupervised image-to-image translation. In *Proceedings of the IEEE/CVF conference on computer vision and pattern recognition*, pages 10785–10794, 2021. 3
- [36] Ze Liu, Yutong Lin, Yue Cao, Han Hu, Yixuan Wei, Zheng Zhang, Stephen Lin, and Baining Guo. Swin transformer: Hierarchical vision transformer using shifted windows. In *Proceedings of the IEEE/CVF international conference on computer vision*, pages 10012–10022, 2021. 3
- [37] I Loshchilov. Decoupled weight decay regularization. *arXiv preprint arXiv:1711.05101*, 2017. 6
- [38] Ilya Loshchilov and Frank Hutter. Sgdr: Stochastic gradient descent with warm restarts. *arXiv preprint arXiv:1608.03983*, 2016. 6
- [39] ZhiYong Lv, HaiTao Huang, Xinghua Li, MingHua Zhao, Jón Atli Benediktsson, WeiWei Sun, and Nicola Falco. Land cover change detection with heterogeneous remote sensing images: Review, progress, and perspective. *Proceedings of the IEEE*, 110(12):1976–1991, 2022. 2
- [40] Zhiyong Lv, Haitao Huang, Weiwei Sun, Meng Jia, Jón Atli Benediktsson, and Fengrui Chen. Iterative training sample augmentation for enhancing land cover change detection performance with deep learning neural network. *IEEE Transactions on Neural Networks and Learning Systems*, 2023.
- [41] Zhiyong Lv, Pingdong Zhong, Wei Wang, Zhenzhen You, Jón Atli Benediktsson, and Cheng Shi. Novel piecewise distance based on adaptive region key-points extraction for lccd with vhr remote-sensing images. *IEEE Transactions on Geoscience and Remote Sensing*, 61:1–9, 2023. 2
- [42] Andrea Meraner, Patrick Ebel, Xiao Xiang Zhu, and Michael Schmitt. Cloud removal in sentinel-2 imagery using a deep residual neural network and sar-optical data fusion. *ISPRS Journal of Photogrammetry and Remote Sensing*, 166:333–346, 2020. 2
- [43] Adam Paszke, Sam Gross, Soumith Chintala, Gregory Chanan, Edward Yang, Zachary DeVito, Zeming Lin, Alban Desmaison, Luca Antiga, and Adam Lerer. Automatic differentiation in pytorch. 2017. 6
- [44] Deepak Pathak, Philipp Krahenbuhl, Jeff Donahue, Trevor Darrell, and Alexei A Efros. Context encoders: Feature learning by inpainting. In *Proceedings of the IEEE conference on computer vision and pattern recognition*, pages 2536–2544, 2016. 3
- [45] Dustin Podell, Zion English, Kyle Lacey, Andreas Blattmann, Tim Dockhorn, Jonas Müller, Joe Penna, and Robin Rombach. Sdxl: Improving latent diffusion models for high-resolution image synthesis. *arXiv preprint arXiv:2307.01952*, 2023. 4
- [46] Alec Radford, Jong Wook Kim, Chris Hallacy, Aditya Ramesh, Gabriel Goh, Sandhini Agarwal, Girish Sastry, Amanda Askell, Pamela Mishkin, Jack Clark, et al. Learning transferable visual models from natural language supervision. In *International conference on machine learning*, pages 8748–8763. PMLR, 2021. 5, 6
- [47] Robin Rombach, Andreas Blattmann, Dominik Lorenz, Patrick Esser, and Björn Ommer. High-resolution image synthesis with latent diffusion models. In *Proceedings of the IEEE/CVF conference on computer vision and pattern recognition*, pages 10684–10695, 2022. 2, 3, 4, 6
- [48] Olaf Ronneberger, Philipp Fischer, and Thomas Brox. U-net: Convolutional networks for biomedical image segmentation. In *Medical image computing and computer-assisted intervention—MICCAI 2015: 18th international conference, Munich, Germany, October 5–9, 2015, proceedings, part III 18*, pages 234–241. Springer, 2015. 2
- [49] Chitwan Saharia, William Chan, Huiwen Chang, Chris Lee, Jonathan Ho, Tim Salimans, David Fleet, and Mohammad Norouzi. Palette: Image-to-image diffusion models. In *ACM SIGGRAPH 2022 conference proceedings*, pages 1–10, 2022. 3
- [50] Michael Schmitt, Lloyd Haydn Hughes, and Xiao Xiang Zhu. The senl-2 dataset for deep learning in sar-optical data fusion. *arXiv preprint arXiv:1807.01569*, 2018. 2, 9
- [51] Christoph Schuhmann, Romain Beaumont, Richard Vencu, Cade Gordon, Ross Wightman, Mehdi Cherti, Theo



- Coombes, Aarush Katta, Clayton Mullis, Mitchell Wortsman, et al. Laion-5b: An open large-scale dataset for training next generation image-text models. *Advances in Neural Information Processing Systems*, 35:25278–25294, 2022. 4
- [52] Alessandro Sebastianelli, Erika Puglisi, Maria Pia Del Rosso, Jamila Mifdal, Artur Nowakowski, Pierre Philippe Mathieu, Fiora Pirri, and Silvia Liberata Ullo. Plfm: Pixel-level merging of intermediate feature maps by disentangling and fusing spatial and temporal data for cloud removal. *IEEE Transactions on Geoscience and Remote Sensing*, 60:1–16, 2022. 2, 3
- [53] Maximilian Seitzer, Arash Tavakoli, Dimitrije Antic, and Georg Martius. On the pitfalls of heteroscedastic uncertainty estimation with probabilistic neural networks. *arXiv preprint arXiv:2203.09168*, 2022. 5, 11
- [54] Minseok Seo, Youngtack Oh, Doyi Kim, Dongmin Kang, and Yeji Choi. Improved flood insights: Diffusion-based sar to eo image translation. *arXiv preprint arXiv:2307.07123*, 2023. 2, 3
- [55] Tamar Rott Shaham, Michaël Gharbi, Richard Zhang, Eli Shechtman, and Tomer Michaeli. Spatially-adaptive pixel-wise networks for fast image translation. In *Proceedings of the IEEE/CVF Conference on Computer Vision and Pattern Recognition*, pages 14882–14891, 2021. 3
- [56] Jacob Shermeyer, Daniel Hogan, Jason Brown, Adam Van Etten, Nicholas Weir, Fabio Pacifici, Ronny Hansch, Alexei Bastidas, Scott Soenen, Todd Bacastow, et al. Spacenet 6: Multi-sensor all weather mapping dataset. In *Proceedings of the IEEE/CVF conference on computer vision and pattern recognition workshops*, pages 196–197, 2020. 3, 6, 9
- [57] Uwe Soergel, Antje Thiele, Hermann Gross, and Ulrich Thoennessen. Extraction of bridge features from high-resolution insar data and optical images. In *2007 Urban Remote Sensing Joint Event*, pages 1–6. IEEE, 2007. 2, 3
- [58] Jiaming Song, Chenlin Meng, and Stefano Ermon. Denoising diffusion implicit models. *arXiv preprint arXiv:2010.02502*, 2020. 6, 10
- [59] Marc Spigai, Céline Tison, and Jean-Claude Souyris. Time-frequency analysis in high-resolution sar imagery. *IEEE Transactions on Geoscience and Remote Sensing*, 49(7):2699–2711, 2011. 3
- [60] Fabio Tosti, Valerio Gagliardi, Fabrizio D’Amico, and Amir M Alani. Transport infrastructure monitoring by data fusion of gpr and sar imagery information. *Transportation Research Procedia*, 45:771–778, 2020. 2
- [61] Thierry Toutin. Three-dimensional topographic mapping with aster stereo data in rugged topography. *IEEE Transactions on geoscience and remote sensing*, 40(10):2241–2247, 2002. 3, 6
- [62] Adam Van Etten. You only look twice: Rapid multi-scale object detection in satellite imagery. *arXiv preprint arXiv:1805.09512*, 2018. 2
- [63] Patrick von Platen, Suraj Patil, Anton Lozhkov, Pedro Cuenca, Nathan Lambert, Kashif Rasul, Mishig Davaadorj, Dhruv Nair, Sayak Paul, William Berman, Yiyi Xu, Steven Liu, and Thomas Wolf. Diffusers: State-of-the-art diffusion models. <https://github.com/huggingface/diffusers>, 2022. 4, 6
- [64] Puyang Wang and Vishal M Patel. Generating high quality visible images from sar images using cnns. In *2018 IEEE Radar Conference (RadarConf18)*, pages 0570–0575. IEEE, 2018. 3
- [65] Yihan Wang, Lahav Lipson, and Jia Deng. Sea-raft: Simple, efficient, accurate raft for optical flow. In *European Conference on Computer Vision*, pages 36–54. Springer, 2025. 5
- [66] Zhou Wang, Alan C Bovik, Hamid R Sheikh, and Eero P Simoncelli. Image quality assessment: from error visibility to structural similarity. *IEEE transactions on image processing*, 13(4):600–612, 2004. 6
- [67] Juan Wei, Huanxin Zou, Li Sun, Xu Cao, Shitian He, Shuo Liu, and Yuqing Zhang. Cfrwd-gan for sar-to-optical image translation. *Remote Sensing*, 15(10):2547, 2023. 3
- [68] Lori White, Brian Brisco, Mohammed Dabboor, Andreas Schmitt, and Andrew Pratt. A collection of sar methodologies for monitoring wetlands. *Remote sensing*, 7(6):7615–7645, 2015. 2
- [69] Rongyuan Wu, Tao Yang, Lingchen Sun, Zhengqiang Zhang, Shuai Li, and Lei Zhang. Seesr: Towards semantics-aware real-world image super-resolution. In *Proceedings of the IEEE/CVF conference on computer vision and pattern recognition*, pages 25456–25467, 2024. 4
- [70] Sidi Wu, Yizi Chen, Samuel Mermet, Lorenz Hurni, Konrad Schindler, Nicolas Gonthier, and Loic Landrieu. Stegogan: Leveraging steganography for non-bijective image-to-image translation. In *Proceedings of the IEEE/CVF Conference on Computer Vision and Pattern Recognition*, pages 7922–7931, 2024. 3, 6, 8, 9, 10
- [71] Yoshio Yamaguchi. Disaster monitoring by fully polarimetric sar data acquired with alos-palsar. *Proceedings of the IEEE*, 100(10):2851–2860, 2012. 2
- [72] Donggeun Yoon, Minseok Seo, Doyi Kim, Yeji Choi, and Donghyeon Cho. Deterministic guidance diffusion model for probabilistic weather forecasting. *arXiv preprint arXiv:2312.02819*, 2023. 3, 6, 8, 9, 10
- [73] Geunhyuk Youk and Munchurl Kim. Transformer-based synthetic-to-measured sar image translation via learning of representational features. *IEEE Transactions on Geoscience and Remote Sensing*, 61:1–18, 2023. 3, 6, 8, 10
- [74] Nir Zabari, Aharon Azulay, Alexey Gorkor, Tavi Halperin, and Ohad Fried. Diffusing colors: Image colorization with text guided diffusion. In *SIGGRAPH Asia 2023 Conference Papers*, pages 1–11, 2023. 4
- [75] Jinsong Zhang, Mengdao Xing, and Yiyuan Xie. Fec: A feature fusion framework for sar target recognition based on electromagnetic scattering features and deep cnn features. *IEEE Transactions on Geoscience and Remote Sensing*, 59(3):2174–2187, 2020. 3
- [76] Jiexin Zhang, Jianjiang Zhou, and Xiwen Lu. Feature-guided sar-to-optical image translation. *IEEE Access*, 8:70925–70937, 2020. 2, 3
- [77] Lvmin Zhang, Anyi Rao, and Maneesh Agrawala. Adding conditional control to text-to-image diffusion models. In *Proceedings of the IEEE/CVF international conference on computer vision*, pages 3836–3847, 2023. 3, 6, 8, 9, 10

- [78] Richard Zhang, Phillip Isola, and Alexei A Efros. Colorful image colorization. In *Computer Vision—ECCV 2016: 14th European Conference, Amsterdam, The Netherlands, October 11–14, 2016, Proceedings, Part III 14*, pages 649–666. Springer, 2016. [3](#)
- [79] Richard Zhang, Jun-Yan Zhu, Phillip Isola, Xinyang Geng, Angela S Lin, Tianhe Yu, and Alexei A Efros. Real-time user-guided image colorization with learned deep priors. *arXiv preprint arXiv:1705.02999*, 2017. [3](#)
- [80] Richard Zhang, Phillip Isola, Alexei A Efros, Eli Shechtman, and Oliver Wang. The unreasonable effectiveness of deep features as a perceptual metric. In *Proceedings of the IEEE conference on computer vision and pattern recognition*, pages 586–595, 2018. [6](#)
- [81] Yueting Zhang, Chibiao Ding, Xiaolan Qiu, and Fangfang Li. The characteristics of the multipath scattering and the application for geometry extraction in high-resolution sar images. *IEEE Transactions on Geoscience and Remote Sensing*, 53(8):4687–4699, 2015. [2](#), [3](#)
- [82] Shihao Zhao, Dongdong Chen, Yen-Chun Chen, Jianmin Bao, Shaozhe Hao, Lu Yuan, and Kwan-Yee K Wong. Uni-controlnet: All-in-one control to text-to-image diffusion models. *Advances in Neural Information Processing Systems*, 36:11127–11150, 2023. [3](#), [6](#), [8](#), [9](#), [10](#)
- [83] Yitao Zhao, Turgay Celik, Nanqing Liu, and Heng-Chao Li. A comparative analysis of gan-based methods for sar-to-optical image translation. *IEEE Geoscience and Remote Sensing Letters*, 19:1–5, 2022. [3](#), [6](#), [9](#)
- [84] Zhi Zhao, Kefeng Ji, Xiangwei Xing, Huanxin Zou, and Shilin Zhou. Ship surveillance by integration of space-borne sar and ais—review of current research. *The Journal of Navigation*, 67(1):177–189, 2014. [2](#)
- [85] Chuanxia Zheng, Tat-Jen Cham, and Jianfei Cai. The spatially-correlative loss for various image translation tasks. In *Proceedings of the IEEE/CVF conference on computer vision and pattern recognition*, pages 16407–16417, 2021. [3](#)
- [86] Jie Zhou, Daniel L Civco, and John A Silander. A wavelet transform method to merge landsat tm and spot panchromatic data. *International journal of remote sensing*, 19(4):743–757, 1998. [6](#)
- [87] Jun-Yan Zhu, Taesung Park, Phillip Isola, and Alexei A Efros. Unpaired image-to-image translation using cycle-consistent adversarial networks. In *Proceedings of the IEEE international conference on computer vision*, pages 2223–2232, 2017. [3](#), [6](#), [8](#), [9](#), [10](#)